Atmospheric Environment 83 (2014) 282–290

Contents lists available at ScienceDirect

Atmospheric Environment

journal homepage: www.elsevier.com/locate/atmosenv

Influence of wind speed on optical properties of aerosols in the marine boundary layer measured by ship-borne DePolarization Lidar in the coastal area of Korea

Dong Ho Shin [a], Detlef Müller [b,c,*], Taejin Choi [d], Young Min Noh [a], Young Jun Yoon [d], Kwon H. Lee [e], Sung Kyun Shin [a], Namyi Chae [d,f], Kwanchul Kim [a], Young J. Kim [a]

[a] School of Environmental Science & Engineering, Gwangju Institute of Science and Technology (GIST), Oryong-dong, Buk-gu, Gwangju 500-712, Republic of Korea
[b] University of Hertfordshire, College Lane, Hatfield AL10 9AB, United Kingdom
[c] Science Systems and Applications, Inc., MS 475 NASA Langley Research Center, Hampton, VA 23681, USA
[d] Korea Polar Research Institute (KOPRI), 26 Songdomirae-ro, Yeonsu-gu, Incheon, Republic of Korea
[e] Department of Geoinformatics Engineering, Kyungil Univ., Gyungsan 712-701, Republic of Korea
[f] Civil and Environmental Engineering, Yonsei University, Yonse-ro, Seodaemun-gu, Seoul 120-749, Korea

HIGHLIGHTS

- Shipborne depolarization aerosol lidar measurements near Korean peninsula.
- Characterization of sea-salt particles with lidar in the eastern Pacific region.
- Correlation of sea-salt optical properties with wind speed provides parameterization.
- Correlation may be caused by duration of transport over the ocean, too.
- Our results are comparable to correlation parameters reported in literature.

ARTICLE INFO

Article history:
Received 3 June 2013
Received in revised form
7 October 2013
Accepted 9 October 2013

Keywords:
Lidar
Aerosol
Wind speed
Marine boundary layer

ABSTRACT

Shipboard measurements of microphysical and optical properties of marine boundary-layer aerosols were performed around the Korean Peninsula from 2 to 5 December 2009. The measurements were conducted aboard the Korean icebreaking research vessel Araon during cruise tracks in the East Sea of Korea near Busan and Pohang. This paper describes the results of optical aerosol measurements acquired with a DePolarization Lidar (DPL) and an optical particle counter (OPC) and data on meteorological parameters. Backward trajectory analyses indicate that two different aerosol characteristics according to different pathways of air mass were encountered during the cruise. We find a high correlation between wind speeds across the east coast of Korea and extinction coefficient, depolarization ratio and mass concentration Correlation coefficient (R^2) are 0.57, 0.52 and 0.67, respectively. The increase of extinction coefficient, depolarization ratio and number concentration with wind speed may have been caused by the increase of sea-salt aerosol production and transport.

1. Introduction

Aerosols play a significant role in air quality and atmospheric visibility. They affect the global climate because of their effect on the solar radiation. The so-called aerosol direct effect occurs when aerosols affect the radiation budget by scattering and absorbing solar radiation (Ayash et al., 2008; Ma et al., 2008). The aerosol indirect effect occurs when the optical properties of clouds are changed by, e.g. cloud condensation and lifetime processes, because of the influence of microphysical and chemical characteristics of aerosols on cloud properties (Goodale and Mansfield, 1987; Twomey et al., 1984).

The ocean is one of the major sources of natural aerosols. On the global scale, the total mass of natural aerosols is much higher than that of anthropogenic aerosols. Sea salt is the strongest natural source of aerosol with a production rate of about 1000–10,000 Tg per year (Winter and Chýlek, 1997). Sea salt aerosols dominate the

* Corresponding author. University of Hertfordshire, College Lane, Hatfield AL10 9AB, United Kingdom. Tel.: +44 (0)1707 28 77803.
E-mail addresses: d.mueller@herts.ac.uk, detlef@tropos.de (D. Müller).

1352-2310/$ – see front matter
http://dx.doi.org/10.1016/j.atmosenv.2013.10.027

atmosphere clear-sky radiative forcing over the oceans (Grini et al., 2002; Ma et al., 2008). Sea salt aerosols act as cloud condensation nuclei (CCN) and modify the radiative properties and lifetime of clouds (Murphy et al., 1998; Pierce and Adams, 2006). Therefore, changes in marine aerosol properties are likely to have important climatological implications (Ayash et al., 2008; Murphy et al., 1998).

The main mechanism leading to the production of sea salt aerosol is air bubbles bursting at the surface of the ocean as a result of wind stress (An et al., 1986; Blanchard, 1983). The bubbles are formed when breaking waves are lifted into the marine boundary layer (MBL) (Blanchard and Syzdek, 1988). Breaking waves create whitecaps and sea-spray droplets that consist of a large number of air bubbles, which is essential for the increased production of marine aerosols (Fairall et al., 1983). As the bubbles fall back to the surface they form whitecaps and burst, thus leading to the injection of sea water film and jet drops into the atmosphere (Resch et al., 1986; Wu, 1990). A correlation is found between surface wind speed and the aerosol concentration of sea salt (Latham and Smith, 1990; O'Dowd and Smith, 1993).

Despite their importance, marine aerosols remain one of the most poorly understood aerosols in the atmosphere. Particularly, the relation between marine aerosol optical properties and wind speed is difficult to quantify because it can be masked by the long-range transport of aerosols that originate from land-based sources (Smirnov et al., 1995; Villevalde et al., 1994) and get mixed into the marine boundary layer.

The main objective of this paper is to investigate the relationship between microphysical and optical properties of marine aerosols along with their variation with wind speed. The paper is organized as follows: Section 2 presents the method and the measurements. Section 3 discusses microphysical and optical properties of the marine aerosols observed in our study. Section 4 summarizes our findings.

2. Measurement and method

We used data from the ship-borne DePolarization Lidar (DPL), an optical particle counter (OPC), and data obtained with hygrometer, thermometer, anemometer, and anemoscope. These instruments were installed aboard the research icebreaking vessel Araon. Araon is operated by the Korea Polar Research Institute (KOPRI). The first cruise of Araon mainly took place along the coast and lasted from 2 to 4 December 2009. Fig. 1 shows the cruise track of Araon. We performed a backward trajectory analyses for aerosol transport characteristics. We identified air masses characteristic of clean marine conditions and air masses that were influenced by anthropogenic aerosols from East Asia.

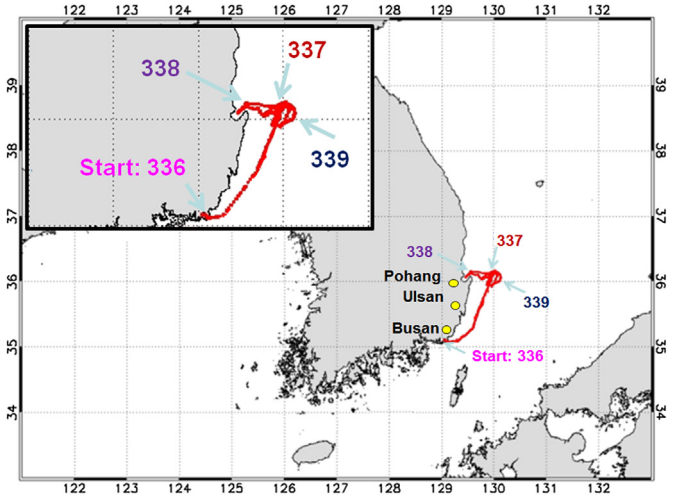

Fig. 1. Cruise track of Araon. The blue numbers are Julian day in 2009 and denote the position of the vessel. (For interpretation of the references to color in this figure legend, the reader is referred to the web version of this article.)

2.1. DePolarization Lidar (DPL)

The DPL system is the first ship-borne lidar of Korea. The system was developed by KOPRI between March 2007 and April 2008. The lidar is installed on an optical table in a way that compensates for vibrations as much as possible. The lidar system is compact in size and it is installed in a container for deployments during cruises on Araon. The seatainer is weatherproof. A tilted, transparent glass roof protects the system against harsh environmental stress such as sea salt particles, exhaust from the Araon engine, ocean waves, precipitation, extreme humidity and temperature changes. The DPL system is operating without maintaining it each day. It can also be remote-controlled from other places through internet. The glass roof was cleaned by hand every few days and after rain during the campaign.

Fig. 2 shows the sketch of the DPL. The DPL system measures profiles of the linear total depolarization ratio (DPR, δ_t) and backscatter coefficients of atmospheric particles at 532 nm wavelength. The light source of the lidar is a pulsed Nd:YAG laser (Quantel CFR400) which operates at the wavelength of 1064 nm. A frequency-doubling crystal allows for generating linear-polarized laser light at 532 nm wavelength. The laser emits pulses of 170 mJ at 532 nm wavelength. The pulse repetition rate is 30 Hz. The laser beam is transmitted vertically into the atmosphere after it is expanded five-fold. This system has a coaxial configuration between the expanded laser beam and the receiver telescope. The backscattered light is collected with an 8-inch Schmidt–Cassegrain telescope. After reflection from the secondary mirror of the telescope, the backscattered light is focused to a pinhole. After passing the pinhole, an achromatic lens collimates and transmits the light

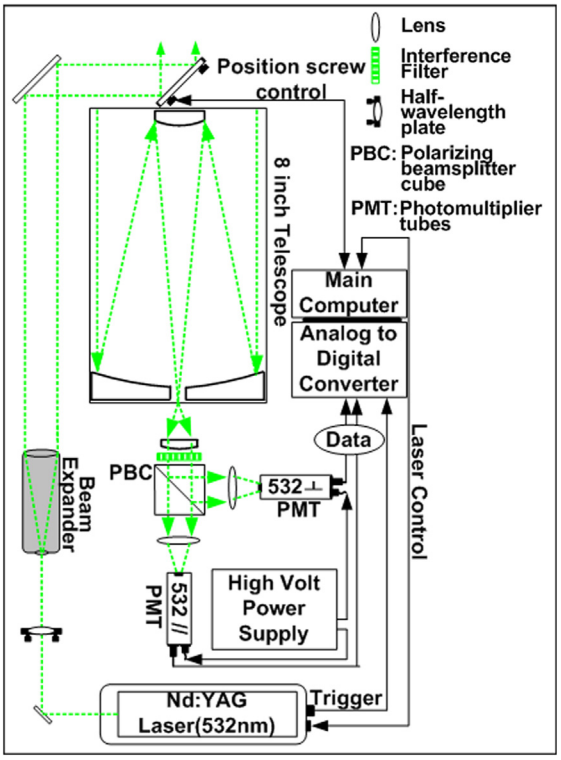

Fig. 2. Schematic layout of the lidar system.

to an interference filter that transmits at 532 nm. The interference filter is placed in front of a polarizing beam splitter cube (PBC). The interference filter reduces the background noise from solar radiation. The PBC is used to separate the parallel from the cross-polarized signals of the depolarized backscatter signals. These two polarized beams then enter photomultiplier tubes (PMT) which generate electronic signals which are subsequently collected by the data acquisition system. The ratio of the gain of the two detectors was determined by rotating a half-wavelength plate. The plate is located at the front end of the laser head. An analog-to-digital converter (ADC) is used to digitize the output from the PMTs. The sampling rate is 60 MHz. Measurements were taken by collecting 3600 laser shots (2 min time resolution) and a vertical resolution of 2.5 m. The lowest height of complete overlap of laser beam and field of view of the receiver telescope is 250 m.

The δ_t indicates if the scattering particles have non-spherical shape (Murayama et al., 2004; Sassen, 1991). The δ_t is defined as the ratio of the cross-polarized lidar return signal with respect to the parallel-polarized backscatter signal (Freudenthaler et al., 2009; Murayama et al., 1999; Sugimoto and Lee, 2006). The δ_t describes the sum of two components, i.e., the molecular DPR (δ_m) and the particle DPR (δ_p). The δ_p can be defined by the following equation:

$$\delta'_p = \left(R\delta'_t - \delta'_m\right)/(R-1) \quad (1)$$

where $\delta' = \delta/(1+\delta)$ (Murayama et al., 1999). The term R denotes the backscatter ratio. We use a constant δ_m of 1.4% (Cairo et al., 1999; Weber et al., 1967).

The uncertainty of δ_p comes from the error of the particle backscatter coefficient of the δ calibration and systematic errors such as the incomplete separation of the linear polarization due to the receiving optics (Cairo et al., 1999; Freudenthaler et al., 2009; Mattis et al., 2009). Using the derived error formulas and estimations of the basic errors (Freudenthaler et al., 2009), the δ_p values have a mean relative uncertainty of 15%.

The vertical optical profiles are derived on the basis of the Klett algorithm (Klett, 1985). Before applying the Klett algorithm, we performed signal smoothing by Savitsky–Golay filters for the random component of the error (Althausen et al., 2000; Whiteman, 1999). Signal smoothing lengths are 50 m for backscatter coefficient and δ. Radiosondes were launched two times a day (00:00 and 12:00 h, UTC) at Pohang (36.03°N, 129.38°E) which is about 20–50 km away from the position of the research vessel. The Klett method needs as input the lidar ratio and the reference value of the

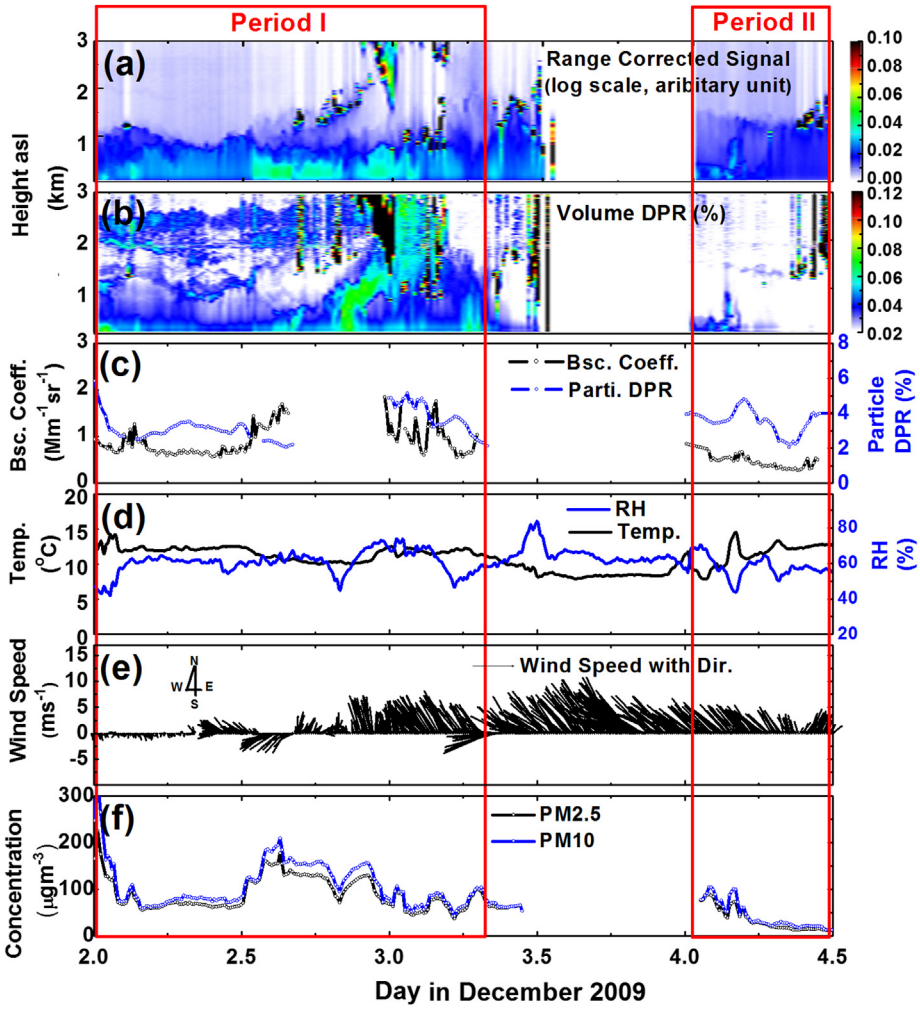

Fig. 3. Temporal changes of the lidar data and the sea surface meteorological data taken between 0000 UTC on 2 December and 1200 UTC on 4 December 2009. We show (a) vertical profiles of the range corrected backscatter signal, (b) the δ_v, (c) the temporal changes of the δ_p and the backscatter coefficients at 300 ± 50 m above sea level, (d) temperature (black line) and relative humidity (blue line), (e) wind speed and direction, and (f) PM2.5 and PM10 concentrations. Periods I and II are identified on the basis of backward trajectory analysis, as discussed in Section 3.2. The gap in the data in Fig. 3(a), (b), (c) and (f) indicates the missing data period caused by precipitation. (For interpretation of the references to color in this figure legend, the reader is referred to the web version of this article.)

particle backscatter coefficient in a specific height in order to derive the profile of the particle backscatter coefficient. The calibration point of the backscatter profile of the raw signals was set in an altitude where no particles but only molecules contributed to the measured signals.

The retrieval of the particle extinction coefficients from the elastic lidar signals significantly depends on the correct choice of the lidar ratio. The lidar ratio is defined as the ratio of the extinction coefficient to the backscatter coefficient. In general, the uncertainty of the profiles of the extinction coefficient that is derived with this type of lidar is larger than the uncertainty of the profiles of the backscatter coefficient. In that regard, we may use information on so-called aerosol types which can be distinguished according to their lidar ratio. We point out that the concept of using aerosol types can be used only as an approximation in data analysis. A clear distinction among aerosol types may only be possible if these types occur in their pure form. Mixing of aerosol types, as it may easily happen in East Asia washes out the clear separation. In our study we used the constant lidar ratio of 23 sr (at 532 nm) for marine aerosols (Müller et al., 2007). In view of the existing literature we acknowledge the possibility that this value may not be characteristic for all types of naturally occurring maritime aerosols. Furthermore, for the calculation of the backscatter coefficient based on the 'standard error propagation equation' (Bevington and Robinson, 1969), we consider signal noise and systematic errors (Ansmann et al., 1992; Gutkowicz-Krusin, 1993). The relative statistical error of the backscatter coefficients is on the order of 5–10% (Althausen et al., 2000; Noh et al., 2009; Tesche et al., 2009).

2.2. Optical Particle Counter (OPC)

Aerosol size distributions and number concentrations were measured with an OPC (Grimm Model 265). The OPC was placed at the bottom of the radar mast, 20 m above sea level. The OPC detects scattered laser-light at a mean scattering angle of 90°. The serial binary signals of the OPC were logged to a PC in the atmospheric lab room which was located on the upper deck of the research vessel. The OPC provided 5-min averaged data of the number size distribution, binned into 31 different size ranges from 0.25 to 32 μm and above (all sizes are given as optically equivalent diameter). The OPC performed continuous sampling of the aerosols from which the size distributions were determined and averaged for the measurement times of the lidar observations. Mass concentrations were calculated from the number size distributions (Burkart et al., 2010; Snider and Petters, 2008). The aerosol density of 2.2 g cm^{-3} for marine aerosol was used in the mass concentration calculation (Fan and Toon, 2010; Tang et al., 1997). Data from the DPL and the OPC measurements were acquired continuously during the cruise. The averaging time of the DPL and OPC was 10 and 5 min, respectively. Measurement data contaminated by the ship exhaust plume were excluded from the data analysis. For this purpose we used information on wind direction. The data were retained when the relative wind direction was within 120° to the left and 60° to the right of the ship heading. Wind directions and other meteorological data such as wind speed, air temperature and relative humidity (RH) were measured at the top of radar mast at 20 m height above sea level.

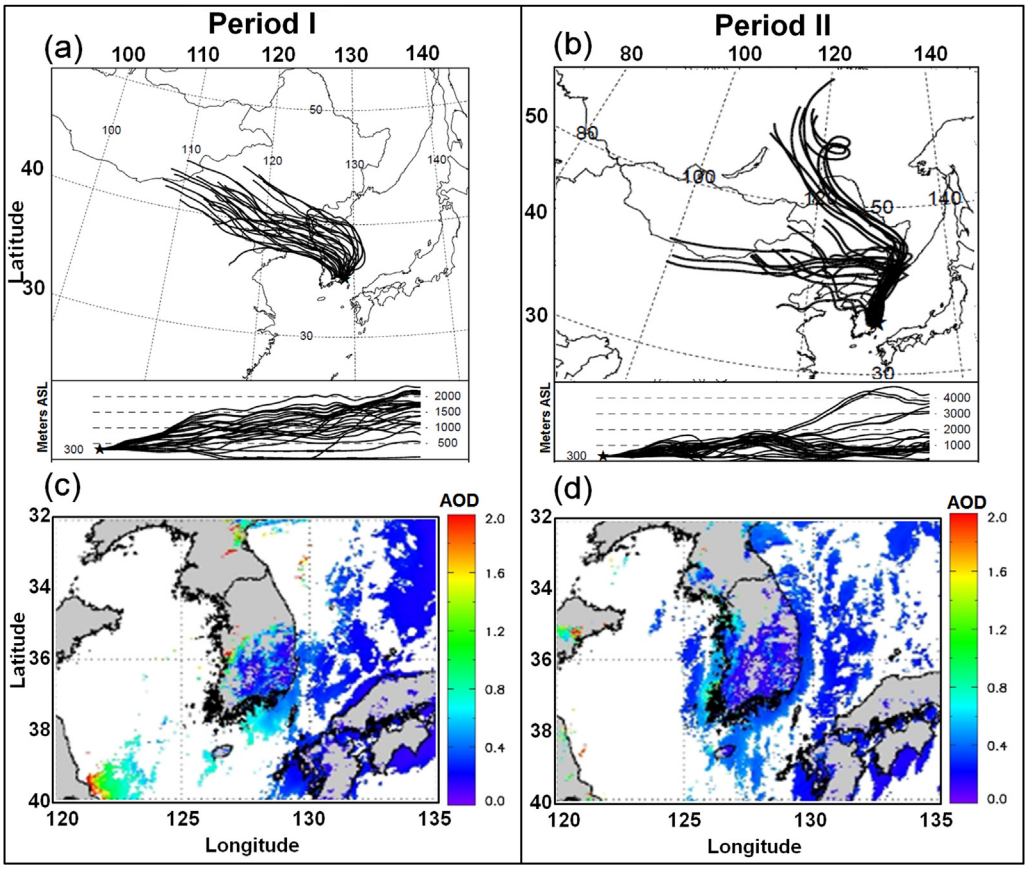

Fig. 4. Four-day backward trajectories of air masses computed with the NOAA/ARL HYSPLIT model for (a) the measurement period I and (b) the measurement period II. Each line represents backward trajectories of two-hour time intervals arriving along the cruise track at 300 m above sea level. The MODIS-derived spatial distribution of aerosol optical depth in (c) on 2 December (period I) and (d) 4 December (period II) is shown, too.

3. Result and discussion

3.1. Meteorological conditions and lidar measurements

Fig. 3 shows the time series of the profiles of the DPL data and the meteorological data. Fig. 3(a) and (b) show the time–height distributions of the range-corrected signals and the δ_m acquired during the entire observation period. Because of precipitation caused by low-level clouds, the lidar measurements were interrupted from 1250 UTC on 3 December to 0010 UTC on 4 December. Temporal variations of the backscatter coefficient and the δ_p at the height of 300 ± 50 m are shown in Fig. 3(c). Note that the measurement of the backscatter coefficient and the δ_p was temporally interrupted from 1500 to 2400 UTC on December 2 and from 1250 UTC on 3 December to 0010 UTC on 4 December, because of the appearance of clouds. Fig. 3(d) and (e) show the temporal variations of the meteorological parameters. The total mass concentration of the aerosol particles is shown in Fig. 3(f). We categorized period I and period II according to the air mass pathways that are shown in Fig. 3 (see Section 3.2).

3.2. Classification of the atmospheric conditions

Backward trajectories were analyzed to understand the air mass transport pathway and the potential source regions of the aerosols encountered during the cruise. We analyzed the aerosol characteristics with respect to categorized back trajectories for our initial estimation of the sources of the aerosols. Four-day backward trajectories in the lower atmosphere were calculated using the HYSPLIT (HYbrid Single-Particle Lagrangian Trajectory) model (Draxler and Rolph, 2003; Rolph, 2003). Air mass backward trajectories that ended along the cruise path were computed for heights of 300 m above sea level (see Fig. 4).

Period I denotes air masses that originated from the Chinese mainland, passed across the Korean Peninsula and then entered the measurement pathway across the line defined by Busan, Pohang and Ulsan (these cities are the biggest harbor and industrial cities in Korea). Period II denotes air masses that originated from the north of China and Siberia and entered the measurement pathway along the east coast of the Korean Peninsula.

Fig. 4(c) and (d) show the MODIS-retrieved AOD at 550 nm obtained by the modified GSTAR algorithm (Lee et al., 2006a,b) for 2 and 4 December 2009. Areas where clouds or sun-glint was present or areas where there was an orbital gap in the data are shown in white. The MODIS AOD over the southeast coast of the Korean peninsula (near the cruise track of Araon; see Fig. 1) during period I shows higher values than the AOD that describes period II.

3.3. Microphysical and optical properties

3.3.1. Vertical profiles

Fig. 5(a) shows the vertical distributions of temperature, virtual potential temperature, and RH obtained from radiosonde data. Fig. 5(b) shows calculated vertical profiles of aerosol backscatter coefficients and the δ_p at 532 nm. The height of the MBL can be determined from the vertical profiles of the aerosol backscatter coefficient (Drobinski et al., 1998), and the base of the inversion layer from the radiosonde data (Barnes et al., 1980; Zeng et al., 2004). The region where the aerosol backscatter coefficient sharply decreases and the potential temperature lapse rate changes can be used as an indicator of the top of the MBL. The slope of the relative humidity profile and the virtual potential temperature profile sharply changes between 1.3 and 1.7 km, which can also be used for identifying the top of the MBL. The aerosol backscatter

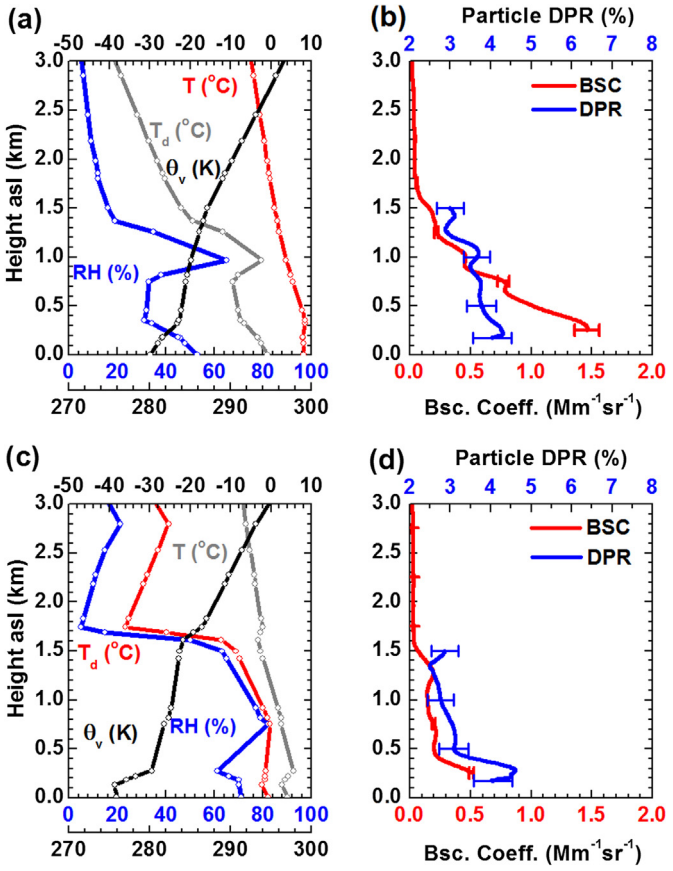

Fig. 5. DPL analysis and radiosonde results obtained (a) and (b) on 2 December 2009, 1200 UTC (Period I), and (c) and (d) 4 December 2009, 0000 UTC (Period II). We show backscatter coefficients and δ_ps based on DPL measurements at 532 nm (b) and (d), and temperature T, virtual potential temperature θ_v, dew point T_d, and relative humidity RH values measured by radiosonde (a) and (c). The error bars indicate 15% error for the backscatter profiles and for the δ_p.

coefficient profiles show that the top of the MBL was at around 1.5 km above sea level.

The height differences of the MBL that we obtain from the two methods can be caused by different definitions that use different

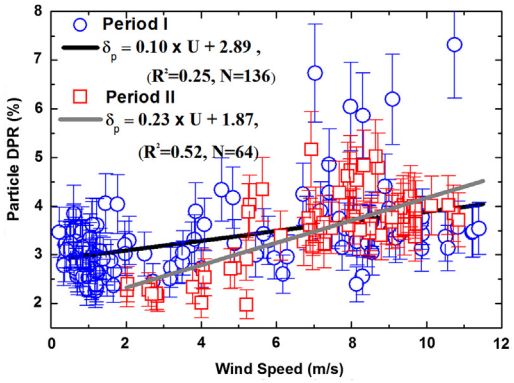

Fig. 6. Variations of the δ_p (532 nm) at 300 ± 50 m height above sea level in dependence of wind speed (U). The open blue circles describe period I; the open red squares describe period II. The bold lines illustrate the linear regression lines of the two periods. The error bars indicate an error of 15% for the δ_p. N and R^2 are the number of measurement points and the correlation coefficients, respectively. (For interpretation of the references to color in this figure legend, the reader is referred to the web version of this article.)

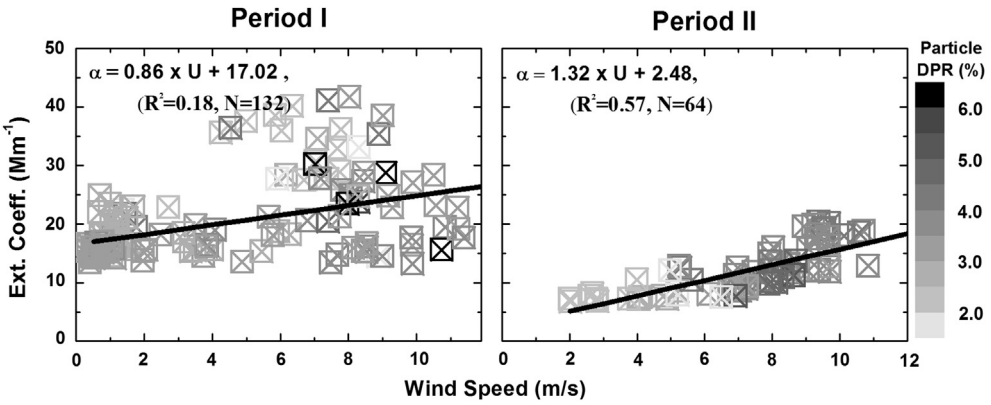

Fig. 7. Dependence of the extinction coefficient (532 nm) at 300 ± 50 m height above sea level versus surface wind speed. The bold black line illustrates the linear regression; the equation and correlation coefficients (R) for the regressions are also shown.

measurement parameters (Baars et al., 2008; Haeffelin et al., 2012). The height of the MBL determined from the temperature profiles measured with radiosonde is in good agreement to the MBL height determined from the aerosol profiles measured with the DPL.

3.3.2. Relationship between wind speed and aerosol optical properties

Fig. 6 indicates a slight dependence of the δ_p with increasing wind speed. Regarding the increase of the δ_p with increasing wind speed, the following causes are possible candidates: (1) soil or dust particles transported from the continent, which can be seen from the back trajectory analysis (see Fig. 4), may be mixed into the MBL; (2) sea-salt particles crystallize by the strong sea breeze.

Soil and sea-salt particles are non-spherical and should increase the δ. Sea-salt particles are hygroscopic. On the one hand, they do not markedly change their shape through uptake of water until 75% RH is reached. On the other hand, humidified sea-salt particles can exist in a supersaturated droplet phase until RH drops below 45–48% (Tang et al., 1977; Tang, 1996; Winkler and Junge, 1971). In this study, during the two-measurement periods, RH was above 40% and below 75% which thus could have allowed for sea-salt particles being more in their crystallized phase and/or more in their droplet phase.

We investigated the correlation of the aerosol extinction coefficient retrieved for the altitude of 300 ± 50 m in dependence of the wind speed for the two measurement periods I and II, respectively, see Fig. 7. We assume that the wind speeds at the two different measurement heights, extinction coefficients were retrived at 300 ± 50 m above sea level and wind speed measurements were taken at 20 m above sea level, are almost equal in the MBL in view of the small roughness lengths over water (Stull, 1988). We used the constant lidar ratio of 23 sr (at 532 nm) for marine aerosols. The following relationship holds for the data shown in the scatter plots of Fig. 7:

$$\text{Period I}: \ \alpha = 0.86 \times U + 17.02 \tag{2}$$

$$\text{Period II}: \ \alpha = 1.32 \times U + 2.48 \tag{3}$$

where α is the extinction coefficient, and U is the wind speed. According to these equations the aerosol extinction coefficients increase with increasing wind speed. However, the air mass pathway during period I most likely contained pollution in contrast to period II see Fig. 4(a) and (b). These differences cause differences of the background aerosol loading: 17.02 and 2.48 in Eqs. (2) and (3), respectively. As a consequence, the aerosol extinction coefficients obtained during period I are higher than during period II for same or similar wind speed. The scatter of the extinction coefficients in dependence of wind speed is considerably smaller in period II compared to the scatter of data points that describe period I.

The slope between the aerosol extinction coefficient and wind speed of period II is about 1.5 times higher compared to the slope for period I. For period I we find an extinction coefficient of ~15 Mm^{-1} for wind speed 0 m s^{-1}. In contrast, the extinction coefficient seems to be significantly lower for wind speed 0 m s^{-1} in period II. Though the regression line indicates a value of 0 Mm^{-1}, we note that extinction coefficient seems to level out to a value of ~5–10 Mm^{-1} for wind speeds below ~5 m s^{-1}. The lack of data points below 5 m s^{-1} does not allow us to make a clear conclusion on this assumption. We note, however, that this value of 5–10 Mm^{-1} would result in an optical depth of 0.005–0.01 for a 1 km shallow, clean MBL and thus would indicate background conditions. Such values have also been reported by Zielinski and Pflug (2007) and Lehahn et al. (2010).

In the case of period I we find a high number concentration of aerosols compared to period II (see Figs. 3(f) and 4(c), (d)). The reason for this difference could be caused by the "purity" of the marine aerosols in the sense that period I was characterized by the influence of continental aerosols, see also the discussion given by Zielinski and Pflug (2007).

More work is required to further homogenize our data. In order to make sure that pure sea-salt is responsible for the observed high DPRs and extinction coefficients at high wind speeds, we need

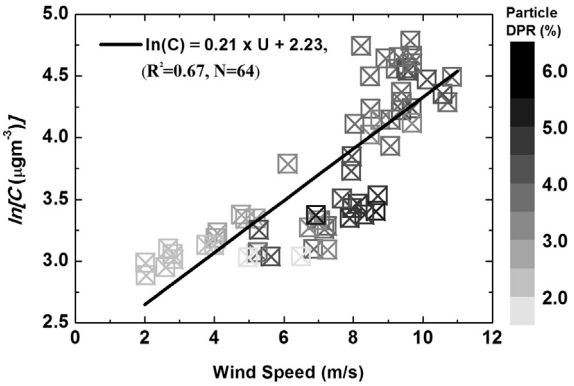

Fig. 8. Scatter plot of the PM10 concentration (μg m^{-3}) on a logarithmic scale versus wind speed (m s^{-1}) of period II.

Table 1
Values of *a*, *b* in Eq. (1) obtained from previous studies.

a (s m^{-1})	b (μg m^{-3})	Sampling height	Region	Measurement time	Reference
0.16	2.57	600 m	Cloud base over Pacific Ocean	1952	Woodcock, 1953
0.16	13.3	15 m	The island of South Uist in the Outer of the Hebrides North Sea, measurement on a platform	1980/1983	Exton et al., 1985
0.16	4.26	5–15 m	Atlantic Ocean, on ship	September 1974–July 1975	Lovett, 1978
0.23	1.13	12 m	Noordwijk in the North Sea, on a research platform (51°S, 4°E)	October–November1986	Marks, 1990
0.21	9.23	20 m	East Sea of Korea (36°N, 129°E)	December 2009	This study
0.27	5.35	1.2 m	1.8 km inland of the Western Indian coast	June–September 1977 and June–August 1978	Kulkarni et al., 1982
0.17	0.64	77 m	Central Western of Hong Kong (residential, location 22.1°N, 114.8°E)		
0.13	0.87	16 m	Sham Shui Po (mixed residential, commercial, industrial, 22.2°N, 114.9°E)	1995–1999	Wai and Tanner, 2004
0.19	0.45	24 m	Yuen Long (residential with fairly rapid urban development, 22.2°N, 114. 1°E)		
0.62	0.33	12–14 m	Pacific Ocean	May, 1964	Tsunogai et al., 1972
0.12	2.52	94 m	Cape Grim, Tasmaniat Cape Grim (41°S, 145°E)	February 1978–May 1980	Gras and Ayers, 1983

more filter samples and chemical analyses (Mayol-Bracero et al., 2002).

3.3.3. *Wind speed dependent mass concentration*

The OPC was used to investigate the relationship between aerosol concentration and wind speed over the Korean coastal area. The generation mechanism of wind-driven sea-salt particles is strongly related to wind speed (Blanchard and Woodcock, 2008; O'Dowd and Smith, 1993). Mass concentrations of sea salt aerosols (C) are expressed by the following equation (Kulkarni et al., 1982; O'Dowd et al., 1997; Wai and Tanner, 2004):

$$\ln(C) = \mathrm{a} \times U + \mathrm{b} \tag{4}$$

The term U is the wind speed, and "a" and "b" are constants. The constant "b" describes the background sea-salt loading or the sea-salt concentration when wind speed reaches zero. This equation implies that the sea salt concentrations are taken from air masses of pure marine origin. Like in previous studies, we find a strong correlation between aerosol concentration and wind speed during period II which describes the situation of a clean marine atmosphere after a precipitation event, see the condition shown in Fig. 8.

According to Equation (4) we obtain a log-linear dependence of the sea-salt concentration with wind speed, i.e.,

$$\ln(C) = 0.21 \times U + 2.23 \tag{5}$$

The values of "a" and "b" from this work are within the range of values found from previous studies, see Table 1 and Fig. 9. There are several reasons that may influence the constants "a" and "b". (1) Different meteorology such as wind speed history, air/sea temperature, salinity and precipitation with geographic location will result in different patterns for sea-salt generation and removal (Gong et al., 1997; Lovett, 1978). (2) The measurement equipment and techniques that are used, such as the sampling time, measured particle size ranges, altitude above sea level of the measurements and measurement sites (Exton et al., 1985).

The value of slope "a" of our study is not significantly different from all other values reported for "a" in previous studies; note the outlier reported by Tsunogai et al. (1972). In contrast, the value "b" may vary across a rather wide range of numbers. The value we obtained for "b" in our study is at the upper end of values reported in literature. The reasons for the high value "b" can be: (1) We performed measurements on a moving ship, which may generate sea-salt particles (Lovett, 1978); (2) large particles which contribute significantly to the sea salt concentration are easy to detect on the surface of the ocean compared to inland measurement (Gong et al., 1997). The residence time of the larger sea salt particles is shorter than the one of small particles due to gravitational settling (Reid et al., 2001; Smith et al., 1993); (3) Sea-salt concentrations are higher in winter than during the other seasons (Gong et al., 1997).

4. Conclusion

Measurements of the optical properties of aerosols in the MBL were carried out along the east coast of Korea during the Araon

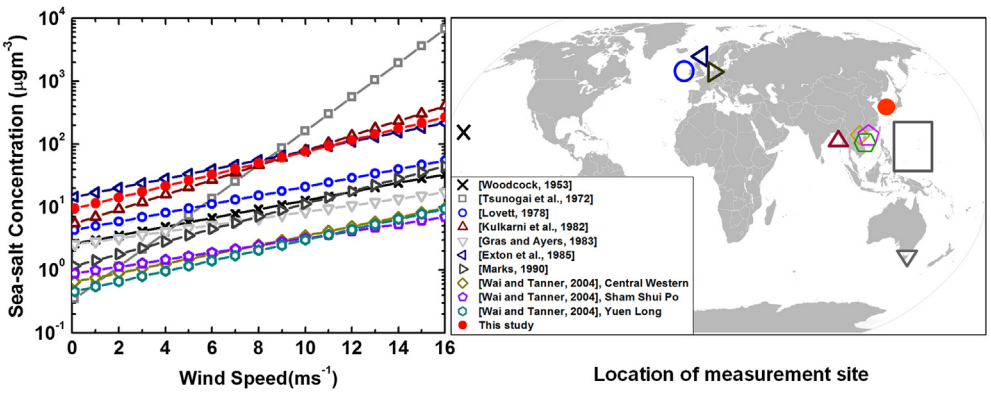

Fig. 9. Comparison of sea-salt mass concentration as a function of wind speed and location of measurement site.

cruise. We used a DePolarization Lidar (DPL), an optical particle counter (OPC) and meteorological instruments. The cruise was from 2 to 5 December 2009.

Different aerosol characteristics were observed and classified according to backward trajectory analyses. The characteristics of aerosol microphysical and optical properties we found during the measurement period are summarized as follows.

(1) We identified two periods that are characterized by two different air mass types. Air masses of period I originated from China and crossed the Korean Peninsula. Accordingly, the air masses were influenced by pollution before they were advected out over the East Korean coastline. In contrast, the air mass of period II passed along the east coast of Korea. In addition this air mass was encountered after a precipitation event.
(2) The lidar vertical profiles show that the backscatter coefficients increase with decreasing height until the overlap region of the lidar is reached.
(3) We reconfirm a log-linear variation of the aerosol number concentration versus wind speed for Period II. In addition, we find that the particle depolarization ratio increases with aerosol number concentration.
(4) The aerosol extinction coefficients increase with increasing wind speed. A linear relationship with a comparably high correlation coefficient is found for wind speed versus particle depolarization ratio in period II. One reason for this increase could be that the sea-salt particles dry off, which would lead to crystallization of the sea-salt and thus result in the increase of the depolarization ratio.

We find different aerosol optical properties during the different periods, in period I, the aerosols are composed of both natural and anthropogenic material. Aerosols of continental origin may have been present in the marine boundary layer. In contrast, the aerosols of period II were comprised mainly of particles of marine origin, i.e. sea salt particles.

In summary, further studies of the scattering properties of sea-salt aerosols under natural conditions with known wind speeds are needed in order to estimate more precisely the net global radiative forcing caused by these aerosol particles.

Acknowledgement

This work was funded by the Korea Meteorological Administration Research and Development Program under Grant CATER 2012-7080. This research was a part of the project titled 'Korea-Polar Ocean in Rapid Transition (KOPRI, PM12020)', funded by the Ministry of Oceans and Fisheries, Korea. This research was supported by the GEMS program of the Ministry of Environment, Korea and the Eco Innovation Program of KEITI (2012000160004). The authors gratefully acknowledge the NOAA Air Resources Laboratory (ARL) for the provision of the HYSPLIT transport and dispersion model and/or READY website (http://www.arl.noaa.gov/ready.php).

References

Althausen, D., Müller, D., Ansmann, A., Wandinger, U., Hube, H., Clauder, E., Zörner, S., 2000. Scanning 6-wavelength 11-channel aerosol lidar. J. Atmos. Ocean. Technol. 17, 1469–1482.
An, E., Spiel, D., Davidson, K., 1986. A Model of Marine Aerosol Generation via Whitecaps and Wave Disruption. In: Oceanic Whitecaps: and Their Role in Air–Sea Exchange Processes, vol. 2, p. 167.
Ansmann, A., Riebesell, M., Wandinger, U., Weitkamp, C., Voss, E., Lahmann, W., Michaelis, W., 1992. Combined Raman elastic-backscatter lidar for vertical profiling of moisture, aerosol extinction, backscatter, and lidar ratio. Appl. Phys. B 55, 18–28.
Ayash, T., Gong, S., Jia, C.Q., 2008. Direct and indirect shortwave radiative effects of sea salt aerosols. J. Clim. 21, 3207–3220.
Baars, H., Ansmann, A., Engelmann, R., Althausen, D., 2008. Continuous monitoring of the boundary-layer top with lidar. Atmos. Chem. Phys. 8, 7281–7296.
Barnes, G., Emmitt, G.D., Brummer, B., LeMone, M.A., Nicholls, S., 1980. The structure of a fair weather boundary layer based on the result of several measurement strategies. Mon. Weather Rev. 108, 349–364.
Bevington, P.R., Robinson, D.K., 1969. Data Reduction and Error Analysis for the Physical Sciences. McGraw-Hill, New York.
Blanchard, D., 1983. The Production, Distribution, and Bacterial Enrichment of the Sea-salt Aerosol. In: Air-sea Exchange of Gases and Particles, pp. 407–454.
Blanchard, D.C., Syzdek, L.D., 1988. Film drop production as a function of bubble size. J. Geophys. Res. 93, 3649–3654.
Blanchard, D.C., Woodcock, A.H., 2008. The production, concentration, and vertical distribution of the sea-salt aerosol. Ann. N. Y. Acad. Sci. 338, 330–347.
Burkart, J., Steiner, G., Reischl, G., Moshammer, H., Neuberger, M., Hitzenberger, R., 2010. Characterizing the performance of two optical particle counters (Grimm OPC1. 108 and OPC1. 109) under urban aerosol conditions. J. Aerosol Sci. 41, 953–962.
Cairo, F., Di Donfrancesco, G., Adriani, A., Pulvirenti, L., Fierli, F., 1999. Comparison of various linear depolarization parameters measured by lidar. Appl. Opt. 38, 4425–4432.
Draxler, R., Rolph, G., 2003. HYSPLIT (HYbrid Single-Particle Lagrangian Integrated Trajectory) Model. NOAA Air Resources Laboratory, Silver Spring. Md. Access via NOAA ARL READY website http://www. arl. noaa. gov/ready/hysplit4. html.
Drobinski, P., Brown, R., Flamant, P.H., Pelon, J., 1998. Evidence of organized large eddies by ground-based Doppler lidar, sonic anemometer and sodar. Bound.-Layer Meteorol. 88, 343–361.
Exton, H., Latham, J., Park, P., Perry, S., Smith, M., Allan, R., 1985. The production and dispersal of marine aerosol. Q. J. R. Meteorol. Soc. 111, 817–837.
Fairall, C., Davidson, K., Schacher, G., 1983. An analysis of the surface production of sea-salt aerosols. Tellus B 35, 31–39.
Fan, T., Toon, O., 2010. Modeling sea-salt aerosol in a coupled climate and sectional microphysical model: mass, optical depth and number concentration. Atmos. Chem. Phys. Discuss. 10, 24499–24561.
Freudenthaler, V., Esselborn, M., Wiegner, M., Heese, B., Tesche, M., Ansmann, A., Müller, D., Althausen, D., Wirth, M., Fix, A., 2009. Depolarization ratio profiling at several wavelengths in pure Saharan dust during SAMUM 2006. Tellus B 61, 165–179.
Gong, S., Barrie, L., Blanchet, J., 1997. Modeling sea-salt aerosols in the atmosphere 1. Model development. J. Geophys. Res. ALL SERIES 102, 3805–3818.
Goodale, M., Mansfield, R., 1987. Climate forcing by anthropogenic aerosols. Neuropsychologia 25, 97.
Grini, A., Myhre, G., Sundet, J.K., Isaksen, I.S.A., 2002. Modeling the annual cycle of sea salt in the global 3D model Oslo CTM2: concentrations, fluxes, and radiative impact. J. Clim. 15, 1717–1730.
Gras, J., Ayers, G., 1983. Marine aerosol at southern mid-latitudes. J. Geophys. Res. 88, 10661–10610.
Gutkowicz-Krusin, D., 1993. Multiangle lidar performance in the presence of horizontal inhomogeneities in atmospheric extinction and scattering. Appl. Opt. 32, 3266–3272.
Haeffelin, M., Angelini, F., Morille, Y., Martucci, G., Frey, S., Gobbi, G., Lolli, S., O'Dowd, C., Sauvage, L., Xueref-Rémy, I., 2012. Evaluation of mixing-height retrievals from automatic profiling lidars and ceilometers in view of future integrated networks in Europe. Bound.-Layer Meteorol. 143, 49–75.
Klett, J.D., 1985. Lidar inversion with variable backscatter/extinction ratios. Appl. Opt. 24, 1638–1643.
Kulkarni, M., Adiga, B., Kapoor, R., Shirvaikar, V., 1982. Sea salt in coastal air and its deposition on porcelain insulators. J. Appl. Meteorol. 21, 350–355.
Latham, J., Smith, M., 1990. Effect on Global Warming of Wind-dependent Aerosol Generation at the Ocean Surface. Nature 347, 372–373.
Lee, K.H., Kim, Y.J., Kim, M.J., 2006a. Characteristics of aerosol observed during two severe haze events over Korea in June and October 2004. Atmos. Environ. 40, 5146–5155.
Lee, K.H., Kim, Y.J., Von Hoyningen-Huene, W., Burlow, J.P., 2006b. Influence of land surface effects on MODIS aerosol retrieval using the BAER method over Korea. Int. J. Remote Sens. 27, 2813–2830.
Lehahn, Y., Koren, I., Boss, E., Ben-Ami, Y., Altaratz, O., 2010. Estimating the maritime component of aerosol optical depth and its dependency on surface wind speed using satellite data. Atmos. Chem. Phys. 10, 6711–6720.
Lovett, R., 1978. Quantitative measurement of airborne sea-salt in the North Atlantic. Tellus 30, 358–364.
Müller, D., Ansmann, A., Mattis, I., Tesche, M., Wandinger, U., Althausen, D., Pisani, G., 2007. Aerosol-type-dependent lidar ratios observed with Raman lidar. J. Geophys. Res. 112, D16202.
Marks, R., 1990. Preliminary investigations on the influence of rain on the production, concentration, and vertical distribution of sea salt aerosol. J. Geophys. Res. 95, 22299–22304.
Ma, X., Von Salzen, K., Li, J., 2008. Modelling sea salt aerosol and its direct and indirect effects on climate. Atmos. Chem. Phys. 8, 1311–1327.
Mattis, I., Tesche, M., Grein, M., Freudenthaler, V., Müller, D., 2009. Systematic error of lidar profiles caused by a polarization-dependent receiver transmission: quantification and error correction scheme. Appl. Opt. 48, 2742–2751.
Mayol-Bracero, O., Gabriel, R., Andreae, M., Kirchstetter, T., Novakov, T., Ogren, J., Sheridan, P., Streets, D., 2002. Carbonaceous aerosols over the Indian Ocean

during the Indian Ocean Experiment (INDOEX): chemical characterization, optical properties, and probable sources. J. Geophys. Res. 107, 8030.
Murayama, T., Müller, D., Wada, K., Shimizu, A., Sekiguchi, M., Tsukamoto, T., 2004. Characterization of Asian dust and Siberian smoke with multi-wavelength Raman lidar over Tokyo, Japan in spring 2003. Geophys. Res. Lett. 31, L23103.
Murayama, T., Okamoto, H., Kaneyasu, N., Kamataki, H., Miura, K., 1999. Application of lidar depolarization measurement in the atmospheric boundary layer: effects of dust and sea-salt particles. J. Geophys. Res. 104, 31781–31792.
Murphy, D., Anderson, J., Quinn, P., McInnes, L., Brechtel, F., Kreidenweis, S., Middlebrook, A., Posfai, M., Thomson, D., Buseck, P., 1998. Influence of sea-salt on aerosol radiative properties in the Southern Ocean marine boundary layer. Nature 392, 62–65.
Noh, Y.M., Müller, D., Shin, D.H., Lee, H., Jung, J.S., Lee, K.H., Cribb, M., Li, Z., Kim, Y.J., 2009. Optical and microphysical properties of severe haze and smoke aerosol measured by integrated remote sensing techniques in Gwangju, Korea. Atmos. Environ. 43, 879–888.
O'Dowd, C.D., Smith, M.H., 1993. Physicochemical properties of aerosols over the northeast Atlantic: evidence for wind-speed-related submicron sea-salt aerosol production. J. Geophys. Res. 98, 1137–1149.
O'Dowd, C.D., Smith, M.H., Consterdine, I.E., Lowe, J.A., 1997. Marine aerosol, sea-salt, and the marine sulphur cycle: a short review. Atmos. Environ. 31, 73–80.
Pierce, J.R., Adams, P.J., 2006. Global evaluation of CCN formation by direct emission of sea salt and growth of ultrafine sea salt. J. Geophys. Res. 111, D06203.
Reid, J.S., Jonsson, H.H., Smith, M.H., Smirnov, A., 2001. Evolution of the vertical profile and flux of large sea-salt particles in a coastal zone. J. Geophys. Res. Atmos. (1984–2012) 106, 12039–12053.
Resch, F., Darrozes, J., Afeti, G., 1986. Marine liquid aerosol production from bursting of air bubbles. J. Geophys. Res. 91, 1019–1029.
Rolph, G., 2003. Real-time Environmental Applications and Display sYstem (READY). NOAA Air Resources Laboratory, Silver Spring. MD. Website http://www. arl. noaa. gov/ready/hysplit4. html.
Sassen, K., 1991. The polarization lidar technique for cloud research: a review and current assessment. Bull. Am. Meteorol. Soc. 72, 1848–1866.
Smirnov, A., Villevalde, Y., O'Neill, N., Royer, A., Tarussov, A., 1995. Aerosol optical depth over the oceans: analysis in terms of synoptic air mass types. J. Geophys. Res. 100, 16639–16650.
Smith, M., Park, P., Consterdine, I., 1993. Marine aerosol concentrations and estimated fluxes over the sea. Q. J. R. Meteorol. Soc. 119, 809–824.
Snider, J.R., Petters, M.D., 2008. Optical particle counter measurement of marine aerosol hygroscopic growth. Atmos. Chem. Phys. 8, 1949–1962.
Stull, R.B., 1988. An Introduction to Boundary Layer Meteorology. Springer, pp. 596–612.
Sugimoto, N., Lee, C.H., 2006. Characteristics of dust aerosols inferred from lidar depolarization measurements at two wavelengths. Appl. Opt. 45, 7468–7474.
Tang, I., Munkelwitz, H., Davis, J., 1977. Aerosol growth studies—II. Preparation and growth measurements of monodisperse salt aerosols. J. Aerosol Sci. 8, 149–159.
Tang, I.N., 1996. Chemical and size effects of hygroscopic aerosols on light scattering coefficients. J. Geophys. Res. 101, 19245–19250.
Tang, I.N., Tridico, A., Fung, K., 1997. Thermodynamic and optical properties of sea salt aerosols. J. Geophys. Res. Atmos. (1984–2012) 102, 23269–23275.
Tesche, M., Ansmann, A., Müller, D., Althausen, D., Mattis, I., Heese, B., Freudenthaler, V., Wiegner, M., Esselborn, M., Pisani, G., 2009. Vertical profiling of Saharan dust with Raman lidars and airborne HSRL in southern Morocco during SAMUM. Tellus B 61, 144–164.
Tsunogai, S., Saito, O., Yamada, K., Nakaya, S., 1972. Chemical composition of oceanic aerosol. J. Geophys. Res. 77, 5283–5292.
Twomey, S.A., Piepgrass, M., Wolfe, T., 1984. An assessment of the impact of pollution on global cloud albedo. Tellus B 36, 356–366.
Villevalde, Y.V., Smirnov, A., O'neill, N., Smyshlyaev, S., Yakovlev, V., 1994. Measurement of aerosol optical depth in the Pacific Ocean and the North Atlantic. J. Geophys. Res. 99, 20983–20988.
Wai, K.M., Tanner, P.A., 2004. Wind-dependent sea salt aerosol in a Western Pacific coastal area. Atmos. Environ. 38, 1167–1171.
Weber, A., Porto, S.P.S., Cheesman, L.E., Barrett, J.J., 1967. High-resolution Raman spectroscopy of gases with cw-laser excitation. J. Opt. Soc. Am. 57, 19–27.
Whiteman, D.N., 1999. Application of statistical methods to the determination of slope in lidar data. Appl. Opt. 38, 3360–3369.
Winkler, P., Junge, C.E., 1971. Comments anomalous deliquescence of sea spray aerosols. J. Appl. Meteorol. 10, 160–163.
Winter, B., Chýlek, P., 1997. Contribution of sea salt aerosol to the planetary clear-sky albedo. Tellus B 49, 72–79.
Woodcock, A.H., 1953. Salt nuclei in marine air as a function of altitude and wind force. J. Metro. 10, 362–371.
Wu, J., 1990. Comment on "Film drop production as a function of bubble size" by DC Blanchard and LD Syzdek. J. Geophys. Res. 95, 7389–7391.
Zeng, X., Brunke, M.A., Zhou, M., Fairall, C., Bond, N.A., Lenschow, D.H., 2004. Marine Atmospheric Boundary Layer Height over the Eastern Pacific: Data Analysis and Model Evaluation. J. Climate 17, 4159–4170.
Zielinski, T., Pflug, B., 2007. Lidar-based studies of aerosol optical properties over coastal areas. Sensors 7, 3347–3365.